Particles I

Access the latest eBook →

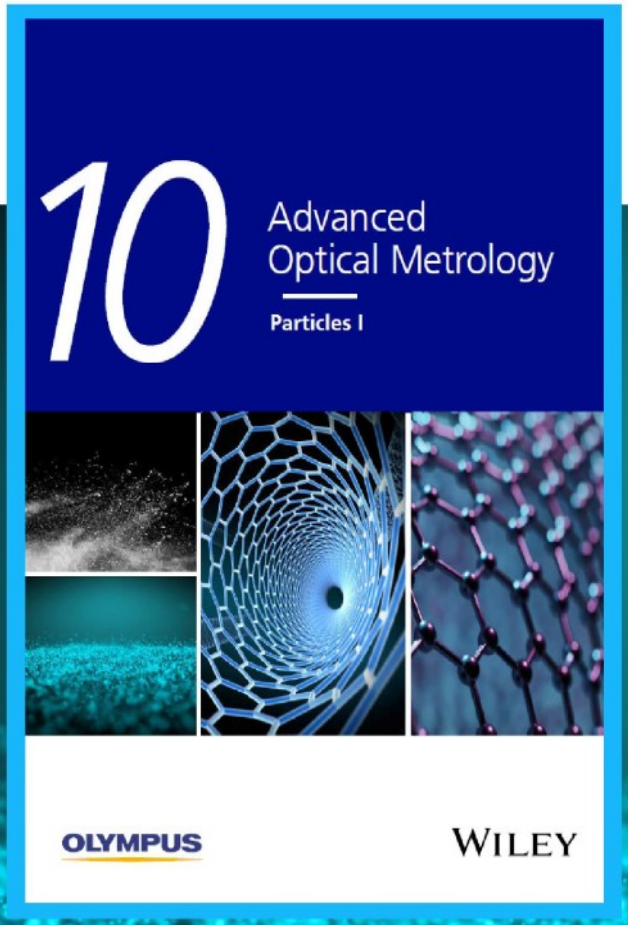

Particles: Unique Properties, Uncountable Applications

Read the latest eBook and better your knowledge with highlights from the recent studies on the design and characterization of micro- and nanoparticles for different application areas.

Access Now

This eBook is sponsored by

OLYMPUS

WILEY

Energy Conversion Analysis of Multi-Layered Triboelectric Nanogenerators for Synergistic Rain and Solar Energy Harvesting

Yang Zheng, Tong Liu, Junpeng Wu, Tiantian Xu, Xiandi Wang, Xun Han, Hongzhi Cui

Xiaofeng Xu, Caofeng Pan*, Xiaoyi Li**

Y. Zheng, T. Liu, J. Wu, T. Xu, Prof. Cui, Prof. X. Xu, Prof. X. Li

College of Materials Science and Engineering, Ocean University of China, Qingdao 266100, China

E-mail: xuxiaofeng@ouc.edu.cn; lixiaoyi@ouc.edu.cn

Y. Zheng, Prof C. Pan

CAS Center for Excellence in Nanoscience, Beijing Key Laboratory of Micro-nano Energy and Sensor, Beijing Institute of Nanoenergy and Nanosystems, Chinese Academy of Sciences, Beijing 101400, P. R. China

E-mail: cfpan@binn.cas.cn

Prof. X. Wang

College of Biomedical Engineering & Instrument Science, Zhejiang University, Hangzhou 310027, China

This article has been accepted for publication and undergone full peer review but has not been through the copyediting, typesetting, pagination and proofreading process, which may lead to differences between this version and the Version of Record. Please cite this article as doi: 10.1002/adma.202202238.

Prof. X. Han

College of Mechatronics and Control Engineering, Shenzhen University, Shenzhen 518060, China

Keywords: (triboelectric nanogenerators, energy conversion analysis, superhydrophobicity, solar cell, hybrid energy harvesting)

Abstract

Triboelectric nanogenerator (TENG) is an emerging technology that offers an excellent potential for the conversion of mechanical energy from rain into electricity for hybrid energy applications. However, a high-performance TENG is yet to be achieved because a quantitative analysis method for the energy conversion process is still lacking. Herein, we present a quantitative analysis method, termed the kinetic energy calculation and current integration (KECCI) method, which significantly improves our understanding of the mechanical-to-electrical energy conversion process. Based on the KECCI method, a high-performance TENG is developed by systematically optimizing a biomimetic surface structure and instant switch design, with 1.25 mA short-circuit current (I_{sc}), 150 V open-circuit voltage (V_{oc}), and a high energy conversion efficiency of 24.89 %. Furthermore, a multi-layered TENG device is proposed for continuously harvesting the kinetic energy of raindrops for further improvement in the energy conversion efficiency. Finally, the multi-layered TENGs are integrated with organic photovoltaics, achieving all-weather energy harvesting. Our work presents a validated theoretical basis that will guide further development of TENGs toward higher performances, which will promote the commercialization of hybrid TENG systems for all-weather applications.

1. Introduction

Harvesting renewable energy from nature has been regarded as the most sustainable solution to the world's energy and environmental problems. [1,2] The mechanical energy from water is currently in the spotlight because of the water's ubiquitous existence and abundance. For example, it is estimated that water can meet approximately 40% of the world's energy demand, which is equal to nearly 800 nuclear power plants. [3] Triboelectric nanogenerator (TENG) is regarded as one of the most effective methods to harvest water energy, especially for the irregular, low-frequency, or micro/nano applications. For areas with a perennial rainy season, raindrop-based TENGs with integrated solar cells represent an ideal solution. Many efforts have been made to fabricate high-performance TENGs for harvesting the mechanical energy from raindrops, waves, and other forms of water. [4–9] Wang et al. enhanced the output performance of a water-based TENG by nano-structures modification, achieving a I_{sc} of 17 μA and a V_{oc} of 9.3 V.[10] An interdigital electrode was designed to increase the output in TENG devices, resulting in a V_{oc} of 23.5 V.[11] Recently, Wang et al. reported a droplet-based electricity generator, which can light 100 LEDs by one droplet. [12] The generator transformed the conventional interfacial effect into a bulk effect, and the instantaneous I_{sc} and V_{oc} of the generator reached 270 μA and 143.5 V, respectively.

However, most of the related research only focuses on the electrical outputs of TENGs, while ignoring the mechanical input energy and the energy conversion process. Recently, an increasing number of researchers are starting to recognize the importance of the input energy and the mechanical impact force at the interface in improving the surface charge density and power output of TENG.[13–17] Niu et al. first established a theoretical model to characterize the TENG output energy. [18] Moreover, Zi et al. reported figure-of-merits as a standard method for defining the performance of TENG.[19] In addition, Xu et al. attempted to describe the force-displacement (F-x) relationship and energy conversion process in TENG systems under ideal conditions.[20] Although considerable efforts are being made to quantify TENG performance, the overall efficiency of the energy conversion process, which begins from the input mechanical energy and ends with the electrical energy output,

cannot be accurately calculated because the relationship between the electrostatic force and displacement has not yet been accurately modeled.[21,22] Meanwhile, the presence of other forces, including conservative forces (spring force, elastic force, gravity, etc.) and dissipative forces (damping force, friction, air resistance, etc.), complicates the energy conversion process. Therefore, the lack of a well-developed theoretical method for the quantitative analysis of the energy conversion efficiency hinders the development of TENG.

In this study, we propose a quantitative method, defined as the kinetic energy calculation and current integration (KECCI) method, to characterize the energy conversion flows, the falling velocity of the droplet, the input mechanical /kinetic energy, the pressure on the friction surface, and the output electrical energy of the TENG. According to this method, there exists an effective pressure (Pe) on the friction surface and an optimal height from which the droplets should fall onto the surface. As a demonstration, we fabricated multi-layered instantaneous-triboelectric nanogenerators (I-TENGs) to repeatedly harvest the kinetic energy of raindrops during the multi-step falling process. Each layer of the TENG contains a superhydrophobic polytetrafluoroethylene (PTFE) film, which is sandwiched between a Pt electrode and an indium tin oxide (ITO)/Ag nanowire composite electrode. The biomimetic microstructure of superhydrophobic PTFE is similar to the lotus leaf structure, consisting of many micro- and nano-sized protrusions.[23] The I_{sc}, V_{oc}, transferred charge, and energy conversion efficiency of I-TENG can reach 1.25 mA, 150 V, 150 nC, and 24.89%, respectively, which are much higher than those reported previously.[10,12,24–26] Finally, a ternary polymer solar cell (PSC) was integrated with the I-TENG in which the active layer contains a small-molecule acceptor with the commercial name Y6, a fullerene acceptor (named PC71BM), and a donor polymer (named PBDB-TF) to harvest both solar and raindrop energy. Such a hybrid energy harvesting system could provide an efficient approach to harvesting energy in different weather conditions.[27,28] The establishment of the energy conversion analysis method (KECCI) and the fabrication of the high-performance multi-layered I-TENGs will significantly improve our

understanding of the mechanical-to-electrical energy conversion process and promote the commercialization of TENG/photovoltaic hybrid energy harvesting systems in the future.

2. Results and discussion

2.1 Structure design, electrical output performance, and working principle of I-TENG

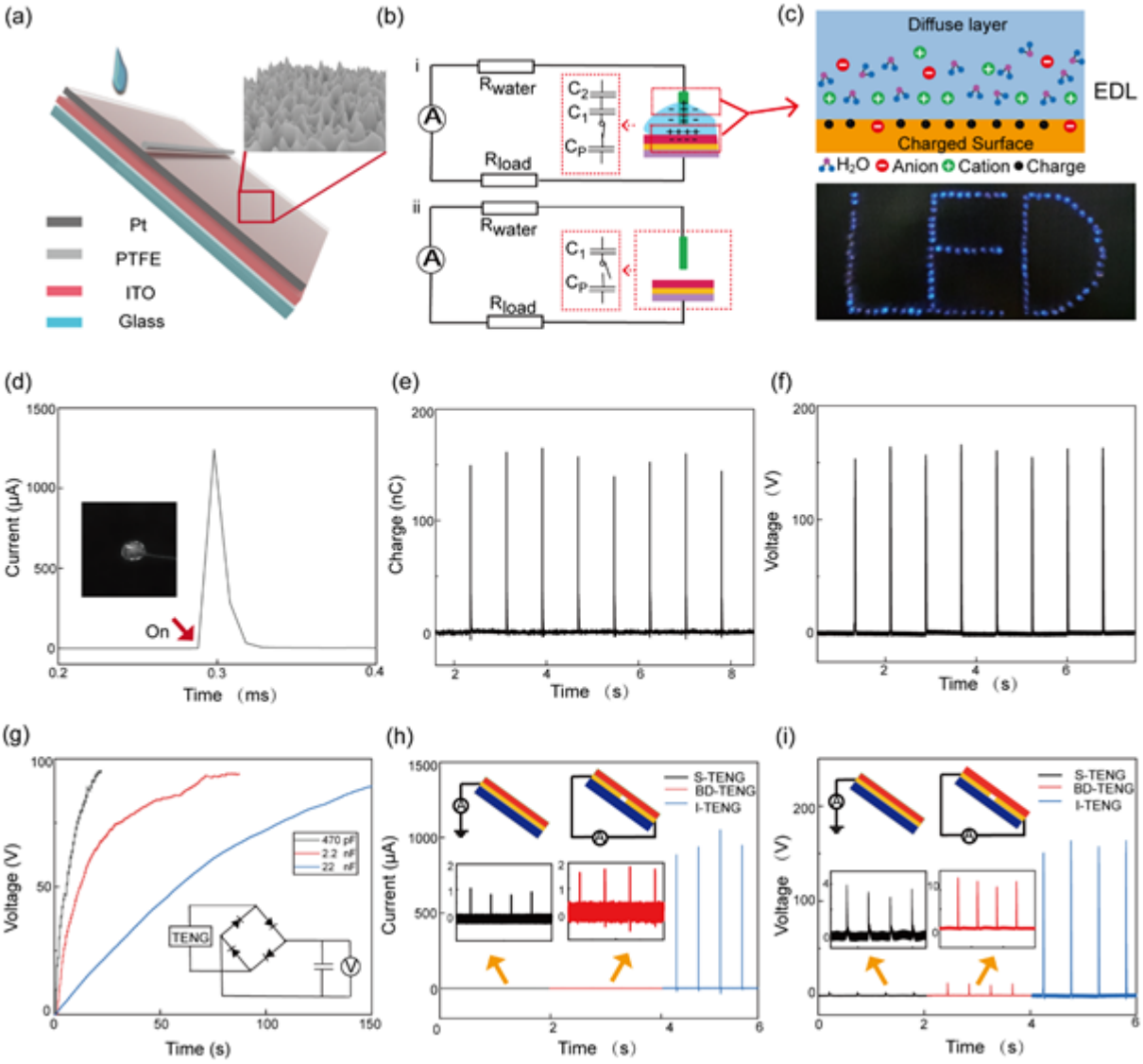

Figure 1. Physical structure and electrical outputs of I-TENG. (a) Structural diagram of I-TENG. (b) Equivalent working circuit diagram of I-TENG. (c) Electric double-layer model and a photograph of I-TENG lighting up 103 blue commercial LEDs with one waterdrop released from 25 cm. (d–f) I_{sc}, transferred charges, and V_{oc} of I-TENG. (g) Voltage curves of charging three commercial capacitors. (h) I_{sc} diagram compared with S-TENG and BD-TENG. (i) V_{oc} diagram compared with S-TENG and BD-TENG.

The instantaneous structure design of the TENG plays an important role in improving its output performance. **Figure 1a** illustrates the structural design of I-TENG with a Pt wire acting as the top electrode and ITO as the bottom electrode. There are many biomimetic structures consisting of micro/nano columnar protrusions on the PTFE surface created by inductively coupled plasma (ICP) etching (**Figure 1a** inset). These bionic structures, which serve as a frictional layer on the PTFE that is similar to the surface structure of lotus leaves, lead to the superhydrophobic performance of the TENG device. The equivalent circuit of the TENG is demonstrated in **Figure 1b**, where a droplet plays the role of a switch. When the ITO and the Pt electrode are not connected by a waterdrop, the switch is at an open state, as shown in **Figure 1bii**. In this condition, the top surface of the PTFE anf the surface of ITO carry triboelectric negative and induced heterogenous positive charges, respectively, which form a capacitor, Cp. Simultaneously, because of the existence of the solid/liquid interface, heterogeneous charges in water will be absorbed on the friction surface to form another capacitor, C1. Because the circuit is open at this time, all of the induced charges are distributed on the ITO electrode, which leads to a voltage difference of hundreds of volts. The equivalent circuit with the switch in the closed state when the waterdrop contacts the Pt electrode, as shown in **Figure 1bi**.

Figure 1c shows an electrical double layer (EDL), which is an electric screening structure that generally forms on any electrode-electrolyte interface. In the I-TENG, there are two EDLs at the liquid/solid interfaces, (the interface of Pt/water and the interface of PTFE/water as indicated by the two rectangles in Figure 1bi) and these EDLs form two capacitors. The EDL at the interface of the PTFE and water forms the first capacitor (C1), while the EDL at the interface of water and the Pt electrode forms the second capacitor, C2. Therefore, the three capacitors (Cp, C1, and C2)and two resistance elements (waterdrop and external resistance) form a closed circuit. Because of the high voltage of the Cp at the open circuit, when a water droplet contacts the Pt electrode and close the circuit, capacitor Cp will charge C2 until their voltage is balanced, as described by Equation 1.

$$V_{cp} = \frac{Q_{cp} \times d_p}{\varepsilon_p \times S_p} = V_{C2} = \frac{Q_{c2} \times d_2}{\varepsilon_2 \times S_2} \quad (1)$$

Where d_p and d_2 are the thichness of Cp and C2, respecvtively; S_p and S_2 are the area of Cp and C2, respectively; ε_p and ε_2 are the charge density of Cp and C2; Q_{c2} and Q_{cp} are charges in Cp and C2.

Due to the thickness of the PTFE, d_p is several orders of magnitude larger than d_2 of the EDL at the water/Pt interfaces, while $\varepsilon_p \times S_p$ and $\varepsilon_2 \times S_2$ are basically of the same order of magnitude. Therefore, Q_{c2} will be much higher than Q_{cp}. This leads to a transfer of the induced charges from the back electrode of ITO to the Pt electrode as the Cp charges C2, with current from ITO to Pt measured through an external circuit. Because of the transient charging process, there will be a very high pulsed current peak, with a duration time of approximately 40 μs (**Figure 1d**). Consequently, according to the equation $I = \frac{Q}{t}$, the instantaneous I_{sc} will be very high when the discharge time (t) is minimal, owing to which the I-TENG output is much higher than that of other similar TENG. [29,30]

For the same reason, when waterdrop leaves the Pt electrode, d_2 can be regarded as infinity, which is much larger than d_p. Thus, V_{C2} will be higher than V_{Cp} and C2 will charge Cp, meaning that the charges will flow back to the ITO electrode through the external circuit, forming a reverse current.

The working principle and enlarged detail of the negative part of the current of I-TENG are shown in **Figure S1** and **S2**, respectively, and the friction process of droplets on PTFE is shown in **Video 1**. As shown in **Figure 1e** and **1f**, when waterdrops fall from a height of 25 cm, the V_{oc} and transferred charge of the device are about 150 V and 150 nC respectively, which is beneficial for some applications of TENG, such as for the purpose of improving the sensitivity of sensors in many fields.[31–35] According to the related research, peak voltage will increase linearly with the thickness of the PTFE film, and the thickness of the PTFE film can be adjusted by controlling the volume of the PTFE precursor and the rotation speed/time of spin coating.[12] Notably, these values are several times higher than that found in other reports, as shown in **Table 1**.

Table 1. Comparison of the electric output values and the overall surface charge density of I-TENG with other devices

Device	I_{sc} (μA)	V_{oc} (V)	Charge (nC)	Area (cm^2)	Charge Density ($\mu C/m^2$)
I-TENG	1250	175	150	3.1	483.87
DEG[12]	300	150	49.8	2.7	184.44
TENG[36]	7.59	37.19	30.59	9	33.99
TENG[10]	17	9.3	1.1	16	0.69
WMAT[37]	70	6		6.15	
IDE-TENG[11]	0.553	23.5	2.2	79.2	0.28
L-L TENG[38]	0.06	4	1	9π	0.35
WD-TENG[39]	32	29.3			
SLIPS-TENG[40]	0.4	1.2	0.18	18.75	0.10

I-TENG can charge a variety of capacitors (e.g., with capacitances of 470 pF, 2.2 nF, and 22 Nf) to approximately 90 V in tens of seconds. To verify the improvement brought by the switch structure mentioned above, similarly structured devices with a single electrode TENG (S-TENG) and a backside double-electrode TENG (BD-TENG) are compared with I-TENG under the same testing conditions. The output I_{sc} and V_{oc} of I-TENG were found to be much higher than those of the S-TENG and BD-TENG (**Figure 1h** and **1i**). These results demonstrate that the instantaneous structure design of the TENG plays an important role in improving its output performance.

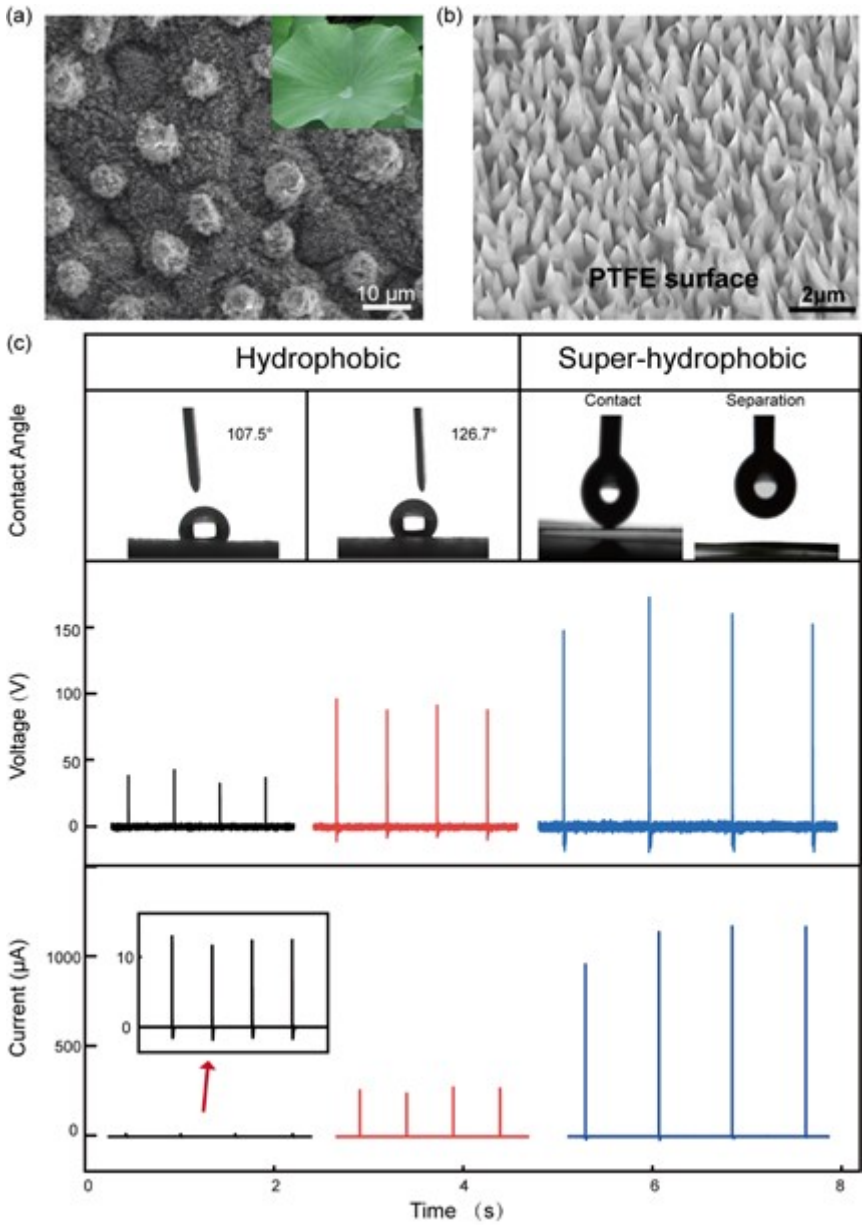

Figure 2. Characterization the surface structure and the outputs of devices with different hydrophobicity. (a) SEM image of lotus leaf (inset is a photograph of lotus leaf). (b) SEM image of superhydrophobic PTFE. (c) Comparison of I_{sc} and V_{oc} of I-TENG fabricated with hydrophobic PTFE (107.5^{o} and 126.7^{o}) and superhydrophobic PTFE.

Because of the existence of two solid/liquid interfaces and two EDLs (**Figure 1b,c)**, the surface properties of the friction material (PTFE) also play important roles in increasing the outputs of TENG. Inspired by the hydrophobic surface of the lotus leaf (**Figure 2a**), we designed the superhydrophobic structure on the PTFE film (**Figure 2b**) to further explicate the relationship between the output performance of the device and the properties of PTFE. According to this idea, PTFE film is etched by inductively coupled plasma (ICP) to achieve its micro/nano columnar protrusion morphology. Fabricating the micro/nano structures with certain roughness on the surface is an effective ways to obtain a superhydrophobic surface.[5,41] It should be noted that the tips of the micro-cones on the surface of PTFE have a diameter of approximately 20 nm, while the diameters of their bases are approximately 670 nm. These dimensions are much lower than those of the nano/microstructure on the lotus micro mastoids (i.e., ~10 μm). Furthermore, the distribution density of the nano/microstructures is hundreds of times greater than that of the lotus leaf, which gives the PTFE its superhydrophobic properties. The waterdrops do not stay on the surface of the superhydrophobic PTFE upon contact, but will stay and form a large contact angle when in contact with an ordinary hydrophobic surface (**Figure 2c**). A comparison of I-TENG outputs under different hydrophobicity clearly indicates that a more hydrophobic surface leads to a higher power output, which is most likely caused by the fact that water can easily leave the small gap between Pt and PTFE (noting that this is also helped by the water's surface tension and capillary effect). The reason that stuck water reduces the efficiency of the devices lies in the fact that the circuit switch remains closed (Figure 1bi), which means that the I-TENG device cannot operate instantaneously as intended. Furthermore, ions in the residual waterdrop will screen the charges on the surface of PTFE, resulting

in a great reduction in the effective charge transfer and output.[42] **Figure S5** in supporting information (SI) shows diagrams of residual droplets of different sizes on the surfaces of TENGs with different hydrophobicity.

According to our experiments and some related research, the micron-sized conical structures on the hydrophobic surface of PTFE have four main functions. First, they increase the surface area of friction materials, which leads to a larger effective friction area. Second, they change the local energy band junction of friction materials at the interface, which leads to a more efficient electron transfer than that in bulk materials.[43–46] Third, they improve the hydrophobicity and reduce the amount of residual liquid at the interface, which prevents the ions from the waterdrop from participating in the formation of the EDLs that reduce the TENG performance. The highly hydrophobic surface can also make the separation step during a contact-separation process more thorough. And fourth, they can reduce residual dust and minerals on the friction surface that can cover the PTFE material and decrease the effective service life of the TENG. In one sentence, in addition to the advantages of the instantaneous structure design, superhydrophobicity also plays an important role in the high-performance outputs of I-TENG.

2.2 Establishment of the relationship between height and outputs of I-TENG.

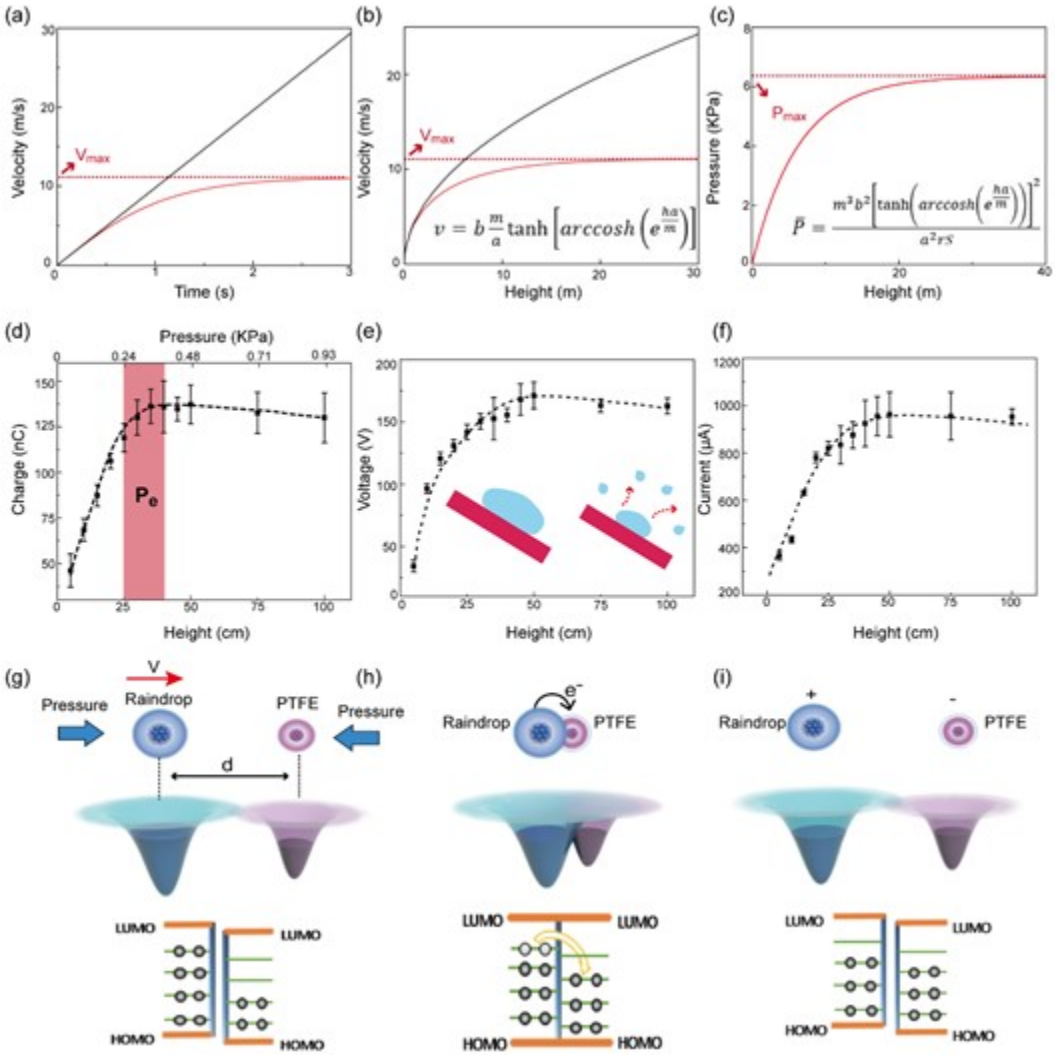

Figure 3. The built of relationship between height and outputs of I-TENG. (a) Relationship between the falling velocity of raindrops and time. (b) Relationship between the falling velocity of raindrops and height of release. (c) Relationship between the pressure of raindrop impact and height of release. (d–f) Transferred charges (d), V_{oc} (e), and I_{sc} (f) as functions of heights of the release of raindrops. (g–i) Electron cloud model and charge transfer for PTFE and waterdrop: (g) before contact, (h) in contact, and (i) after contact.

In addition to the instantaneous structure design and bionic surface features mentioned above, the height of release of waterdrops also has a great impact on the output of TENG. Different heights correspond to different kinetic energies of the waterdrops (i.e., part of the input energy of the

system), which results in different pressures upon the impact of the drops on the device. A comprehensive analytical method that considers both the input (mechanical) and output (electrical) energies is urgently needed to understand the whole energy conversion process in TENGs. To quantitatively study the input energy of waterdrops falling from a certain height, as well as the pressure during the friction process and the electrical energy output, a kinetic energy calculation and current integration (KECCI) method is proposed that encapsulates the relationships among all mentioned parameters. As shown in **Figure 3a,b** by the black lines, the falling velocity of the droplet increases with both time and height under the condition of no air resistance. However, when air resistance is present (i.e., in reality), the falling velocity of raindrops is approximately 10 m s^{-1}. Therefore, any model developed for this purpose should account for air resistance and predict the actual velocity. According to Newton's first law, the velocity or acceleration of a droplet can be described as follows:

$$m\frac{dv}{dt} = mg - F_r \quad (2)$$

where m is the mass of one raindrop, v is the velocity of the raindrop, g is gravitational acceleration, and F_r is the viscous resistance of the raindrop. For a diameter of a middle-sized raindrop of approximately 4.8 mm (volume of 61 μL), F_r can be expressed as follows:

$$F_r = 0.25\pi\rho r^2 v^2 \quad (3)$$

where ρ is the air density and r is the droplet radius. [47]

To simplify Equation 3, a constant a is defined as $a = 0.25\pi\rho r^2$. Integration of Equation 2 then yields:

$$\int \left(-\frac{m}{a}\right)\frac{1}{v^2 - \frac{gm}{a}}dv = \int dt \quad (4)$$

The relationship between the velocity of raindrops (v) and the falling time (t) is given by:

$$v = \sqrt{\frac{gm}{a}\tanh\left(\sqrt{\frac{ga}{m}}t\right)} \quad (5)$$

Furthermore, the relationship between the falling height (h) and falling time (t) is expressed as:

$$t = \frac{arccosh\left(e^{-\frac{ha}{m}}\right)}{b} \quad (6)$$

Finally, the relationship between v and h is expressed as follows (noting that the full derivation process in presented in **Supporting note 1**):

$$v = b\frac{m}{a}\tanh\left[arccosh\left(e^{\frac{ha}{m}}\right)\right] \quad (7)$$

where the droplet mass, m, is 0.061g; the gravitational acceleration, g, is 9.8 m s^{-2}, and b is a constant defined as $b = \sqrt{\frac{ga}{m}}$.

The relationships between v and t and between v and h were calculated according to Equations 5 and 7, respectively. As shown by the red lines in **Figure 3a,b** in the falling process, water droplets first go through an acceleration phase and then reach an extreme value Vmax of approximately 10.2 m s^{-1} (with an error of 3–6% with simulated velocity in other studies).[48,49] Combining Equation 7 with the equation describing the momentum

$$\bar{F}t' = mv \quad (8)$$

the relationship between the pressure of raindrops falling on I-TENG and the falling height is expressed by Equation 9 (noting that the full derivation process is presented in Supporting note 1 in SI).

$$\bar{P} = \frac{m^3b^2\left[\tanh\left(arccosh\left(e^{\frac{ha}{m}}\right)\right)\right]^2}{a^2rS} \quad (9)$$

where S is the spread area of water drops.

Figure 3c illustrates that the pressure of raindrops on the device surface will increase until the raindrop velocity reaches its extreme value, at which point the pressure will also reach a maximum value, Pmax. According to previous studies, the pressure between two friction materials will significantly affect the magnitude of interfacial friction and charge transfer mechanism. Therefore, we then measured the V_{oc}, I_{sc}, and transferred charges of the I-TENG device as waterdrops fell onto the device after being released from different heights (i.e., from 5 to 100 cm). The voltage, current, and charge all increase sharply with an increase in height from 5 to 25 cm. With the height exceeding 25 cm, all measured parameters exhibit a slowed rate of increase until reaching a global maximum at approximately 50 cm. With the height exceeding 50 cm, all electrical parameters present a small downward trend (**Figure 3d–f**). The water drop optimal falling height for maximum output of TENG is affected by several factors, e.g. surface structure, inclination angle, and volume of the droplets.[50,51]We speculate that some droplets break up into smaller pieces due to the high velocity (**Figure 3e** inset), which reduces the contact area between the remaining droplets and the I-TENG surface, thus resulting in less charge transfer. It should be noted that the pressure of approximately 0.3 kPa corresponds to the highest output of the I-TENG. This pressure is defined as the Effective Pressure (Pe), which indicates that the output value does not always increase with increasing pressure/height. Therefore, there exists a threshold effective pressure that is affected by several factors, such as surface tension and the angle of incidence. The impact pressure affects the amount of electron transfer between water drops and PTFE. At the nanoscale, the distance between the water molecule and PTFE molecule will be reduced under the impact pressure, resulting in a higher probability of charge transfer. To illustrate, Figure 3 shows the electron clouds of waterdrops and PTFE at the atomic scale before contact (part g), during contact (part h), and after contact (part i). When the fall height of one droplet varies from 0 to 100 cm, the corresponding pressure varies from

0 to 930 Pa, as shown in Figure 3d. Using this data, we can establish the relationship between transferred charges Q (in nC) and pressure P (in Pa), as follows:

$$Q = \begin{cases} 0.39P + 28.86 & 0 \le P \le 240\ Pa \\ \frac{-112.15}{1+\exp[(P-131.37)/63.33]} + 136.04 & 240 \le P \le 480\ Pa \\ -0.02P + 145.22 & P > 480\ Pa \end{cases} \quad (10)$$

To the best of our knowledge, this is the first time that a model has been presented to calculate how the pressure on a TENG surface affects the transfer of charge, which establishes a mathematical relationship between pressure and transferred charges and sets up a method for a systematic quantitative characterization of the TENG input/output energies.

2.3 Design of multi-layered structured I-TENG and energy calculation.

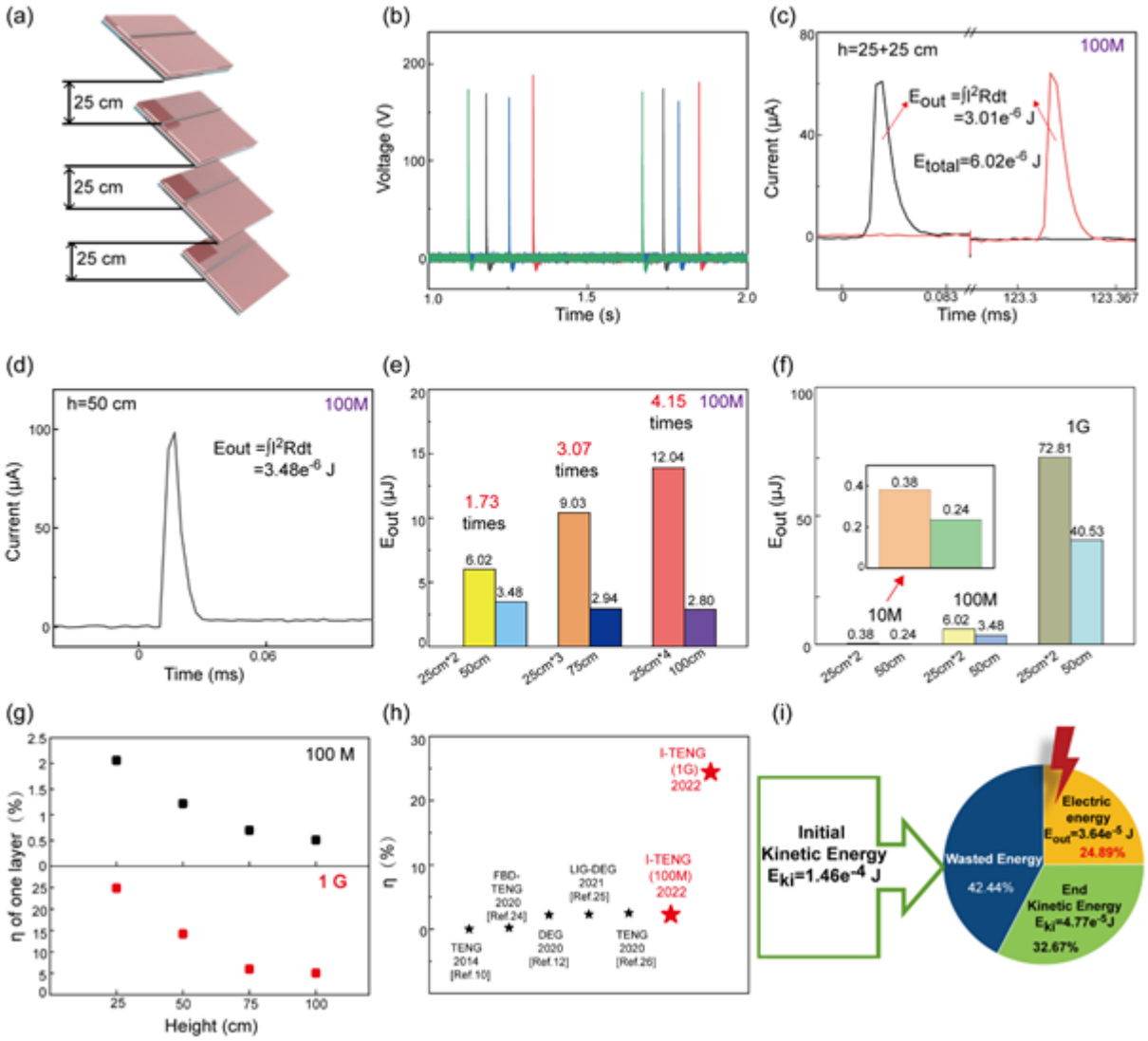

Figure 4. Output energy of multi-layered structured I-TENG. (a) Design diagram of a multi-layered structure. (b) V_{oc} of each layer as measured by four channels of the oscilloscope. (c) I_{sc} and output energy of a two-layer device with a height interval of 25 cm. (d) I_{sc} and output energy of a one-layer device with a height of 50 cm. (e) Comparison of output energy of I-TENG with different height intervals. (f) Comparison of output energy of I-TENG under different external circuit loads. (g) Conversion efficiency of I-TENG with an external load of 100 MΩ (black) and 100 GΩ (red) under different heights. (h) Comparison of conversion efficiency value in our work with other reports.[10,12,24–26] (i) Energy conversion diagram.

The discussions above demonstrate that only a little part of potential energy is converted into kinetic energy and that only a small part of the kinetic energy is converted into electric energy when raindrops fall from a high altitude. In other words, most of the geopotential energy is wasted! To alleviate this problem, we used a multi-layered structure that allows for an intermediate stepped water collection process in which water is initially collected by the topmost layer of the setup before being allowed to drip down onto the additional I-TENG layers (**Figure 4a**). With a total of four layers and a layer separation of 25 cm, this setup drastically improves the total energy generation and the energy conversion efficiency. When a droplet falls from a height of 100 cm, the four layers of the I-TENG generate the signals shown in **Figure 4b**. To demonstrate the benefits of the multi-layered structure, the harvested electrical energies by two layers of I-TENG (with a falling distance of 25 cm) and one layer of I-TENG (with a falling distance of 50 cm) are compared under controlled conditions. The output electrical energy is calculated by integrating the current signals as follows:

$$E_{out} = \oint V\, dQ = \int I^2 R\, dt \qquad (11)$$

According to related research, the TENG's voltage has a serious measurement error, owing to the mismatch of impedance between the instrument and nanogenerator devices. Therefore, it will be more accurate when utilizing the integration of current rather than voltage to calculate the TENG output energy.[52] Under an external load of 100 MΩ, a two-layer device with a layer separation of 25 cm generates output energy for one droplet of $E_{total} = 6.02\, e^{-6}$ J (calculated from Equation 11), while a one-layer device with a falling height of 50 cm generates$E_{out,50} = 3.48\, e^{-6}$ J. These calculations are shown in parts c and d of **Figure 4**. The output energy of the two-layer device is nearly twice that of the one-layer device, which means that a two-layer device can generate more electrical energy than a one-layer device under the same conditions.

Additionally, we calculated the electrical energy output of the I-TENG with different numbers of layers. For heights of 50, 75, and 100 cm, the corresponding device structures are made into two,

three, and four layers, respectively, which are then compared with the single-layer devices. As illustrated in **Figure 4e**, when a droplet fell from a height of 75 cm, the output energy of the three-layer I-TENG was 3.07 times higher than that of the one-layer device. Consistent with this, when a droplet fell from a height of 100 cm, the output energy of the four-layer device was 4.15 times higher than that of the one-layer device.

Furthermore, the external circuit loads will also affect the output energy and output peak power, showing that the electrical output of I-TENG will increase as the external resistance increases for both a two-layer structure and a single-layer structure (**Figure 4f and Figure S7**), which is consistent with previous research of the TENG output performance with different loads.[53,54] With an external load of 100 MΩ, the energy conversion efficiency is calculated to be 2.06%, while a load of 1 GΩ allowed for conversion efficiency of 24.88%. These calculations were based on one water droplet of 61μL being released from a height of 25 cm. Notably, the energy conversion efficiency could reach as high as 36.91% (with a load of 1 GΩ) when the efficiency is calculated using $\eta = E_{out}/E_{ki} - E_{ke}$, where E_{ki} and E_{ke} are the initial and final kinetic energies of raindrops (**Figure S9a**). Although the energy conversion efficiency will decline with an increase in height (**Figure 4g**), the multi-layered design plays an important role in keeping the efficiency always at a relatively high level, as shown in **Figure S8**. A comparison of the energy conversion efficiency of the I-TENG with other reports is shown in **Figure 4h,** clearly demonstrating that the efficiency of the I-TENG is much higher than that of the previously reported droplet-based TENGs. Finally, according to the KECCI method, the entire energy conversion process begins with the kinetic input energy and ends with the electrical output energy, which is demonstrated in **Figure 4i**. Therefore, it is hoped that this method will provide a standard for the quantification of input and output energy, as well as the theoretical analysis model for TENGs and similar systems.

2.4 Hybrid system composed of I-TENG and PSC.

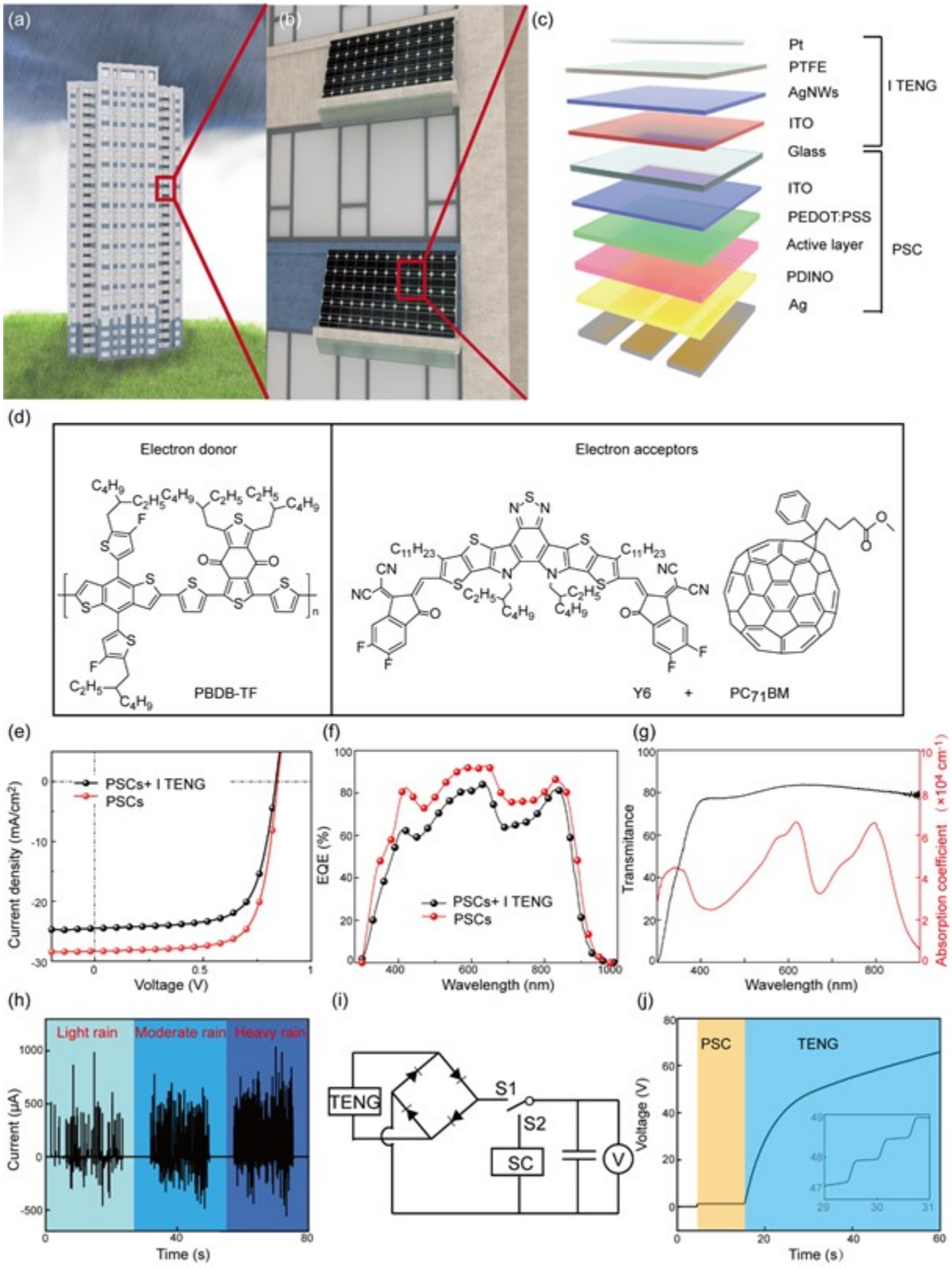

Figure 5. Hybrid system composed of I-TENG and PSC. (a–c) Schematic illustration of modern buildings equipped with the hybrid system composed of I-TENG and solar cells. (d) Chemical structures of conjugated materials in PSCs. (e) *J*–*V* and (f) corresponding EQE curves of PSCs. (g) Transmittance of I-TENG and absorption coefficient of the active layer in PSCs. (h) I_{sc} of I-TENG under three different simulated precipitation densities. (i) Diagram of the charging circuit. (j) Voltage curves of a commercial capacitor charging process that uses PSC and I-TENG.

The benefits of the multi-layered structure remind us of similar examples that are already being utilized in the designs of some existing structures and technologies, including modern residential buildings that are equipped with sloping solar panels located on the outside of each floor. Therefore, it is wise to design a multi-layered hybrid energy harvesting system as an all-weather energy harvester consisting of PSCs and I-TENGs for harvesting both solar and rain energy. An example of such a design is illustrated in **Figure 5a–c**, where the top part of the hybrid device is the I-TENG containing a transparent PTFE film, while the bottom part is a polymer solar cell (PSC). A glass plate can be installed under each platform to ensure that the waterdrops coming from an upper hybrid device can fall directly onto the lower hybrid device, as shown in **Figure S13**.

In addition, the PSCs (the bottom part) with a device configuration of ITO/PEDOT: PSS/active layer/PDINO/Ag were fabricated as the substructure in the hybrid system. The chemical structures of the donor poly[(2,6-(4,8-bis(5-(2-ethylhexyl-3-fluoro)thiophen-2-yl)-benzo[1,2-*b*:4,5-*b*']dithiophene))-*alt*-(5,5-(1',3'-di-2-thienyl-5',7'-bis(2-ethylhexyl)benzo[1',2'-*c*:4',5'-*c*']dithiophene-4,8-dione)] (PBDB-TF), the small-molecule acceptor with the commercial name Y6 and the fullerene acceptor (named $PC_{71}BM$) are depicted in **Figure 5d**. The alternating polymer PBDB-TF and the small molecular Y6 are the state-of-the-art donor and acceptor materials used in PSCs, respectively. $PC_{71}BM$ was used as the third component to form ternary blends in the active layer of PSCs.[55–57]

Figure 5e shows a plot of the current density−voltage (*J*−*V*) curves of the ternary PSCs under one sun (AM 1.5 G, 1000 W cm^{-2}). PSC showed an V_{oc} of 0.83 V, a short-circuit current density (J_{sc}) of 28.3 mA cm^{-2} and a fill factor (FF) of 0.73, leading to a high power-conversion efficiency (PCE) of 17.1%, which is among the best-performing PSCs that are constructed from PBDB-TF:Y6 blends. Notably, the hybrid I-TENG/PSC device retained a high PCE of 14.4 %, with a lower J_{sc} and FF being due to the 80% transmittance of I-TENG in a broad wavelength range of 400−900 nm as shown in **Figure 5g** (black line). The efficiency of solar cell could be enhanced by increasing the transmittance of TENG and fabricating particular nano-structures, which will reduce the reflection loss of light on the surface and thus improve the PCE of solar cell.[36,39] Meanwhile, it should be emphasized that the superhydrophobic surface of the TENG will prevent dust from staying on the surface and always provide a clean surface, ensuring the standard conversion efficiency of the solar cell. The spectral response of PSCs was characterized using external quantum efficiencies (EQEs) (**Figure 5f**). All PSCs presented broad EQE profiles ranging from 300 to 1000 nm, which was in good agreement with the absorption of the ternary blend (**Figure 5g** red line). The photocurrent densities that were calculated by integrating the EQE spectra with an AM 1.5G solar spectrum were consistent with the corresponding J_{sc}, exhibiting low mismatches of within 5%. The results validate the accuracy of the photocurrent densities measured from the *J*−*V* characterization. The hybrid energy harvester was tested under different raindrop densities, i.e., light, moderate, and heavy rain, as shown in **Figure 5h**. The results of that testing yielded approximately the same magnitude of the output current for each rain intensity but a noticeably higher current density at higher rain intensities. This means that the device offers good performance for both heavy and light rain conditions. The hybrid energy harvesting system compensates for some of the losses experienced by the solar cells in cloudy and rainy weather, thus illustrating the advantages of all-weather energy harvesting. As shown in **Figure 5i,j**, on sunny days, when switch is in the S2 position, the hybrid energy harvesting system quickly charges a capacitor to 3 V (as shown in the yellow segment). If the weather changes and it starts to

rain, the switch goes into position S1 and the capacitor is charged by the hybrid energy harvester from 3 to 65 V (as shown in the blue segment). TENG and solar cell are independent parts of the hybrid system, therefore TENG will not break down the solar cell. Long-term stability characterization of I-TENG and PSC are shown in **Figure S16** and **S17**. This high-performance hybrid energy harvesting device provides a new strategy for collecting energy from multiple natural sources, thus promoting the industrialization of the TENG technology.

3. Conclusion

We developed an instantaneous triboelectric nanogenerator (I-TENG) consisting of biomimetic surface structures and an instant switch structural design that improves the outputs of previous TENG devices by more than 10 times. The biomimetic surface structures, which are similar to the micro/nano mastoid structures of lotus leaves, play important roles in increasing the surface charge density and reducing the residue of liquid at the interface. The V_{oc}, I_{sc}, transferred charges and energy conversion efficiency of I-TENG were 150 V, 1.25 mA, 150 nC, and 24.89%, respectively. Furthermore, we introduced a quantitative analysis method (KECCI) to advance our understanding of the energy flows in TENG systems and to guide the development of a multi-layered structural design for such systems. The key advantage of a multi-layered I-TENG is that it can harvest the energy of a raindrop several times in succession to significantly improve the energy conversion efficiency. Finally, we designed a hybrid energy harvesting system composed of high-performance I-TENGs and a PSC to harvest rain and solar energy alternately. In future work, pressure and charge transfer at the atomic level can be further accurately characterized under real rainfall conditions (such as trajectory and angle of incidence of each drop). This research represents a milestone in establishing the quantitative analysis of the energy conversion process of TENGs and in comprehensively understanding the working principles of TENGs. Furthermore, it provides strategies for the design

and fabrication of high-efficiency devices, thereby accelerating the TENG commercialization process and further helping to reduce carbon dioxide emissions in the future.

4. Experimental Section/Methods

4.1 *Materials and fabrication of I-TENG*

Ethanol (Sinopharm, 95%), AgNWs (XFNANO, 10 mg ml-1), ITO coated glass (GLI, 100100), PTFE precursor (Aladdin, 60 wt% dispersion; Chemours, 856G-300) and commercial PTFE film. To fabricate the I-TENG, a piece of ITO glass of size 30×30×2 mm was cleaned in pure water and ethanol. The AgNWs were then deposited on the surface of ITO and a copper wire was connected to the ITO/AgNWs composited electrode. The PTFE film is fabricated onto the AgNWs/ITO electrode by attaching the PTFE film or spin-coating the PTFE precursor under 1000 rpm for 60 s. The PTFE precursor fabricated device was heated at 100 ^{o}C for 10 min to remove all solvent in the PTFE precursor and was then heated at a hot panel of about 380 ^{o}C for 40 min. The thickness of the PTFE film can be adjusted by controlling the volume of the PTFE precursor and the rotation speed/time of spin coating. Finally, a Pt wire was placed on the PTFE layer as the counter electrode. Inductively coupled plasma (ICP) reactive ion etching was applied to produce micro/nano columnar protrusion morphology on the PTFE surface.[5]

4.2 *Measurements and characterizations*

The ionic concentration of tap water used in this experiment was 5 mM. A syringe pump and an injection plastic tube were used to generate droplets and control the volume at 61 μL, which was determined by the inner diameter of the injection needle. The I-TENG was fixed at an angle of 45° against a glass plate. Droplet release height was varied from 5 cm to 100 cm. The I_{sc} of I-TENG was measured by a low-noise current amplifier (Stanford Research System Model SR570) and an oscilloscope (Rohde and Schwarzrte, RTA4004). Charge transfer and V_{oc} were measured by Keithley

6514 electrometer and an oscilloscope RTA4004 equipped with a high-impedance (10 MΩ) probe, respectively. In all measurements, the environment temperature and relative humidity were kept at approximately 50% and 20 ^{o}C, respectively.

Acknowledgments

Y. Zheng and T. Liu contributed equally to this work. The research was supported by the Fundamental Research Funds for the Central Universities, China (Grant No.202112011), National Natural Science Foundation of China (Grant No.52101390, 52125205, U20A20166, 61805015 and 61804011), Natural Science Foundation of Shandong Province, China (ZR2021QE043 and ZR2020ZD33), Natural Science Foundation of Beijing Municipality (Z180011), Shenzhen Science and Technology Program (KQTD20170810105439418), Taishan Scholar Program of Shandong Province, China (tsqn201812026).

Conflict of Interset

The authors declare no conflict of interest.

References

[1] S. Chu, A. Majumdar, *Nature* **2012**, *488*, 294.

[2] Z. L. Wang, *Nature* **2017**, *542*, 159.

[3] X. Wang, S. Niu, Y. Yin, F. Yi, Z. You, Z. L. Wang, *Adv. Energy Mater.* **2015**, *5*, 1501467.

[4] X. Liang, T. Jiang, Y. Feng, P. Lu, J. An, Z. L. Wang, *Adv. Energy Mater.* **2020**, *10*, 2002123.

[5] X. Li, J. Tao, X. Wang, J. Zhu, C. Pan, Z. L. Wang, *Adv. Energy Mater.* **2018**, *8*, 1800705.

[6] Z. Yuan, C. Wang, J. Xi, X. Han, J. Li, S.T. Han, W. Gao, C. Pan, *ACS Energy Lett.* **2021**, *6*, 2809.

[7] X. Li, J. Tao, J. Zhu, C. Pan, *APL Mater.* **2017**, *5*, 074104.

[8] G. Chen, N. Li, J. He, L. Qiao, F. Li, S. Wang, L. Yu, P. Murto, X. Li, X. Xu, *J. Mater. Chem. A* **2020**, *8*, 24664.

[9] X. Wang, M. Que, M. Chen, X. Han, X. Li, C. Pan, Z. L. Wang, *Adv. Mater.* **2017**, *29*, 1605817.

[10] Z. H. Lin, G. Cheng, S. Lee, K. C. Pradel, Z. L. Wang, *Adv. Mater.* **2014**, *26*, 4690.

[11] B. K. Yun, H. S. Kim, Y. J. Ko, G. Murillo, J. H. Jung, *Nano Energy* **2017**, *36*, 233.

[12] W. Xu, H. Zheng, Y. Liu, X. Zhou, C. Zhang, Y. Song, X. Deng, M. Leung, Z. Yang, R. X. Xu, Z. L. Wang, X. C. Zeng, Z. Wang, *Nature* **2020**, *578*, 392.

[13] J. Fu, X. Xia, G. Xu, X. Li, Y. Zi, *ACS Nano* **2019**, *13*, 13257.

[14] X. Li, G. Xu, X. Xia, J. Fu, L. Huang, Y. Zi, *Nano Energy* **2019**, *56*, 40.

[15] X. Wang, Y. Zhang, X. Zhang, Z. Huo, X. Li, M. Que, Z. Peng, H. Wang, C. Pan, *Adv. Mater.* **2018**, *30*, 1706738.

[16] H. Wu, N. Mendel, S. van der Ham, L. Shui, G. Zhou, F. Mugele, *Adv. Mater.* **2020**, *32*, 2001699.

[17] W. Du, X. Han, L. Lin, M. Chen, X. Li, C. Pan, Z. L. Wang, *Adv. Energy Mater.* **2014**, *4*, 1301592.

[18] S. Niu, Y. Liu, S. Wang, L. Lin, Y. S. Zhou, Y. Hu, Z. L. Wang, *Adv. Mater.* **2013**, *25*, 6184.

[19] Y. Zi, S. Niu, J. Wang, Z. Wen, W. Tang, Z. L. Wang, *Nat. Commun.* **2015**, *6*, 8376.

[20] G. Xu, X. Li, X. Xia, J. Fu, W. Ding, Y. Zi, *Nano Energy* **2019**, *59*, 154.

[21] J. Shao, T. Jiang, W. Tang, L. Xu, T. W. Kim, C. Wu, X. Chen, B. Chen, T. Xiao, Y. Bai, Z. L. Wang, *Nano Energy* **2018**, *48*, 292.

[22] Y. K. Pang, X. H. Li, M. X. Chen, C. B. Han, C. Zhang, Z. L. Wang, *ACS Appl. Mater. Interfaces* **2015**, *7*, 19076.

[23] S. Liu, X. Liu, G. Zhou, F. Qin, M. Jing, L. Li, W. Song, Z. Sun, *Nat. Commun.* **2020**, *11*, 6158.

[24] H. Wu, Z. Chen, G. Xu, J. Xu, Z. Wang, Y. Zi, *ACS Appl. Mater. Interfaces* **2020**, *12*, 56060.

[25] Y. Chen, B. Xie, J. Long, Y. Kuang, X. Chen, M. Hou, J. Gao, S. Zhou, B. Fan, Y. He, Y.T. Zhang, C. P. Wong, Z. Wang, N. Zhao, *Adv. Mater.* **2021**, *33*, 2104290.

[26] H. Wu, N. Mendel, D. Van Den Ende, G. Zhou, F. Mugele, *Phys. Rev. Lett.* **2020**, *125*, 078301.

[27] N. Li, L. Qiao, J. He, S. Wang, L. Yu, P. Murto, X. Li, X. Xu, *Adv. Funct. Mater.* **2021**, *31,* 2008681.

[28] Q. Tang, H. Zhang, B. He, P. Yang, Nano Energy **2016**, *30*, 818.

[29] X. Li, X. Ning, L. Li, X. Wang, B. Li, J. Li, J. Yin, W. Guo, Nano Energy **2022**, *92*, 106705.

[30] X. Wang, S. Fang, J. Tan, T. Hu, W. Chu, J. Yin, J. Zhou, W. Guo, Nano Energy **2021**, *80*, 105558.

[31] Y. Liu, R. Bao, J. Tao, J. Li, M. Dong, C. Pan, *Sci. Bull.* **2020**, *65*, 70.

[32] K. Zhou, Y. Zhao, X. Sun, Z. Yuan, G. Zheng, K. Dai, L. Mi, C. Pan, C. Liu, C. Shen, *Nano Energy* **2020**, *70*, 104546.

[33] J. Li, Z. Yuan, X. Han, C. Wang, Z. Huo, Q. Lu, M. Xiong, X. Ma, W. Gao, C. Pan, *Small Sci.* **2022**, *2*, 2100083.

[34] X. Han, Z. Xu, W. Wu, X. Liu, P. Yan, C. Pan, *Small Struct.* **2020**, *1*, 2000029.

[35] C. Wang, R. Ma, D. Peng, X. Liu, J. Li, B. Jin, A. Shan, Y. Fu, L. Dong, W. Gao, Z. L. Wang, C. Pan, *InfoMat* **2021**, *3*, 1272.

[36] L. Zhao, J. Duan, L. Liu, J. Wang, Y. Duan, L. Vaillant-Roca, X. Yang, Q. Tang, *Nano Energy* **2021**, *82*, 105773.

[37] S. H. Kwon, J. Park, W. K. Kim, Y. Yang, E. Lee, C. J. Han, S. Y. Park, J. Lee, Y. S. Kim, *Energy Environ. Sci.* **2014**, *7*, 3279.

[38] J. Nie, Z. Wang, Z. Ren, S. Li, X. Chen, Z. Lin Wang, *Nat. Commun.* **2019**, *10*, 2264.

[39] X. Liu, K. Cheng, P. Cui, H. Qi, H. Qin, G. Gu, W. Shang, S. Wang, G. Cheng, Z. Du, *Nano Energy* **2019**, *66*, 104188.

[40] W. Xu, X. Zhou, C. Hao, H. Zheng, Y. Liu, X. Yan, Z. Yang, M. Leung, X. C. Zeng, R. X. Xu, Z. Wang, *Natl. Sci. Rev.* **2019**, *6*, 540.

[41] L. Feng, S. Li, Y. Li, H. Li, L. Zhang, J. Zhai, Y. Song, B. Liu, L. Jiang, D. Zhu, *Adv. Mater.* **2002**, *14*, 1857.

[42] X. Li, T. H. Lau, D. Guan, Y. Zi, *J. Mater. Chem. A* **2019**, *7*, 19485.

[43] M. Chen, X. Li, L. Lin, W. Du, X. Han, J. Zhu, C. Pan, Z. L. Wang, *Adv. Funct. Mater.* **2014**, *24*, 5059.

[44] X. Li, J. Tao, W. Guo, X. Zhang, J. Luo, M. Chen, J. Zhu, C. Pan, *J. Mater. Chem. A* **2015**, *3*, 22663.

[45] W. Guo, X. Li, M. Chen, L. Xu, L. Dong, X. Cao, W. Tang, J. Zhu, C. Lin, C. Pan, Z. L. Wang, *Adv. Funct. Mater.* **2014**, *24*, 6691.

[46] S. Zuo, P. Chen, C. Pan, *Rare Metals*, **2020**, *39*, 1113.

[47] S. Xu, J. Cui, X. Ren, presented at EMEIT-2012, Applied Mechanics and Engineering Model on Raindrops falling. Atlantis Press, 9, 2012.

[48] A. I. J. M. van Dijk, L. A. Bruijnzeel, C. J. Rosewell, J. Hydrol. **2002**, *261*, 1.

[49] S. Niu, X. Jia, J. Sang, X. Liu, C. Lu, Y. Liu, J Appl Meteorol Climatol **2010**, *49*, 632.

[50] L. Wang, Y. Song, W. Xu, W. Li, Y. Jin, S. Gao, S. Yang, C. Wu, S. Wang, Z. Wang, *EcoMat* **2021**, *3*, 12116.

[51] Q. Zhang, C. Jiang, X. Li, S. Dai, Y. Ying, J. Ping, *ACS Nano* **2021**, *15*,12314.

[52] J. An, P. Chen, C. Li, F. Li, T. Jiang, Z. L. Wang, *Nano Energy* **2022**, *93*, 106884.

[53] L. Ma, R. Wu, S. Liu, A. Patil, H. Gong, J. Yi, F. Sheng, Y. Zhang, J. Wang, J. Wang, W. Guo, Z. L. Wang, Adv. Mater. **2020**, *32*, 2003897.

[54] R. Zhang, C. Dahlström, H. Zou, J. Jonzon, M. Hummelgård, J. Örtegren, N. Blomquist, Y. Yang, H. Andersson, M. Olsen, M. Norgren, H. Olin, Z. L. Wang, *Adv. Mater.* **2020**, *32*, 2002824.

[55] N. Zhang, T. Jiang, C. Guo, L. Qiao, Q. Ji, L. Yin, L. Yu, P. Murto, X. Xu, *Nano Energy* **2020**, *77*, 105111.

[56] Q. Wei, W. Liu, M. Leclerc, J. Yuan, H. Chen, Y. Zou, *Sci. China Chem.* **2020**, *63*, 1352.

[57] R. Yu, H. Yao, Y. Cui, L. Hong, C. He, J. Hou, *Adv. Mater.* **2019**, *31*, 1902302.

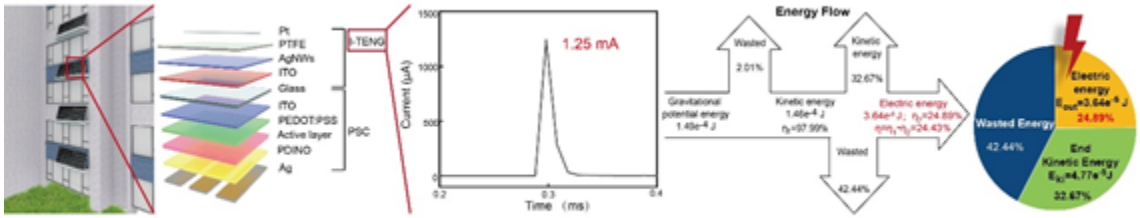

A high-performance I-TENG and a quantitative analysis method (KECCI) are developed to promote the capability of understanding the energy flows and the working principles of TENGs in-depth. In addition, multi-layered TENGs are integrated with organic photovoltaics to harvest the rain and solar energy synergistically. This work guides further development of TENG and promotes its commercialization process.